The Interaction of a Deep Western Boundary Current and the Wind-Driven Gyres as a Cause for Low-Frequency Variability

CAROLINE A. KATSMAN

Royal Netherlands Meteorological Institute, Oceanographic Research, De Bilt, Netherlands, and Institute for Marine and Atmospheric Research Utrecht, Utrecht University, Utrecht, Netherlands

SYBREN S. DRIJFHOUT

Royal Netherlands Meteorological Institute, Oceanographic Research, De Bilt, Netherlands

HENK A. DIJKSTRA

Institute for Marine and Atmospheric Research Utrecht, Utrecht University, Utrecht, Netherlands

(Manuscript received 23 November 1999, in final form 27 November 2000)

ABSTRACT

Recent modeling and observational studies have indicated that the interaction of the Gulf Stream and the deep western boundary current (DWBC) in the North Atlantic may induce low-frequency (decadal timescale) variability. To understand the origin of this low-frequency variability, a line of studies is continued here addressing the stability and variability of the wind-driven circulation using techniques of dynamical systems theory. In an idealized quasigeostrophic 2-layer model setup, stationary solutions of the coupled wind-driven gyres/DWBC system are computed, using the lateral friction as control parameter. Simultaneously, their stability is assessed. When a DWBC is absent, only oscillatory instabilities with intermonthly timescales are found. However, when the strength of the DWBC is increased, the coupled 2-layer flow becomes susceptible to instabilities with interannual timescales. By computing transient flows at relatively low friction, it is found that the existence of these interannual modes induces low-frequency variability in the coupled Gulf Stream/DWBC system with a preferred interannual timescale.

1. Introduction

Near Cape Hatteras, where the Gulf Stream leaves the North American coast and flows eastward into the Atlantic, it crosses the deep western boundary current (DWBC) flowing southward at greater depths. Both observations and numerical studies suggest a strong dynamical interaction between the two currents, resulting in complex behavior of the flow in this crossover region. Richardson (1977) gave an overview of records of Gulf Stream and deep undercurrent measurements collected between 1961 and 1972. Estimates of the undercurrent transport, measured over periods of typically a few weeks, varied between 2 and 50 Sv (Sv $\equiv 10^6$ m^3 s^{-1}), with a mean value of 16 Sv. Hogg (1983) showed that the deep circulation in the crossover area consists of two components: the DWBC flowing southward along the continent and transporting approximately 12 Sv, and two recirculation gyres aligned with the Gulf Stream axis. He argued that these recirculation gyres are driven by eddy momentum fluxes caused by Gulf Stream and DWBC instabilities. In Pickart and Smethie (1993), it was reported that, while the shallowest part of the DWBC (at 500–1200 m depth) is entrained by the Gulf Stream and follows an eastward course, the deeper waters (at 2500–3500 m) do cross underneath the Gulf Stream and stay close to the western boundary of the basin. Recent Lagrangian observations obtained with RAFOS floats launched at approximately 800 and 3000 m depth support this view of the vertical splitting of the DWBC in the crossover region (Bower and Hunt 2000a,b). From surveys conducted over the period 1991–95 a total mean DWBC transport of 19 Sv is deduced, of which 8 Sv is carried in the upper part, and 11 Sv in the deeper part of the DWBC (Pickart and Smethie 1998). Current meter data covering a period of three years were analyzed by Pickart (1994). These observations indicate that on timescales shorter than a year vacillations of the velocity of the DWBC can be attributed to pulsing of the DWBC transport and to meandering of the DWBC itself. On longer timescales, it

Corresponding author address: Caroline A. Katsman, Royal Netherlands Meteorological Institute, Oceanographic Research, P.O. Box 201, 3730 AE De Bilt, Netherlands.
E-mail: katsman@phys.uu.nl

appears that fluctuations in the DWBC are connected to those of the Gulf Stream.

The observational record is still fairly short and, hence, can only give limited information on the characteristics of the variability on longer timescales (see Pickart 1994). In contrast, ocean models can be applied to study the variability of the interacting Gulf Stream and DWBC on both shorter and longer timescales. For example, Thompson and Schmitz (1989) and Tansley and Marshall (2000) demonstrated the strong impact of the DWBC on both the mean path of the Gulf Stream and on (the variability of) its separation point. Using a three-layer primitive equation model of the Gulf Stream/DWBC system, Spall (1996a,b) found pronounced low-frequency variability. The circulation in his model comprised a Gulf Stream–like surface circulation and a shallower and deeper DWBC, and its mean state agreed well with the available observations (Pickart and Smethie 1993). Oscillations with a timescale of 10 years were clearly present in the model simulations. During the high-energy phase of such an oscillation, the DWBC in the second layer is deflected by the Gulf Stream and flows eastward. During the opposite phase, it is only partly deflected and partly remains near the coast and crosses underneath the Gulf Stream. In the upper layer, the Gulf Stream penetrates far into the basin during the high-energy phase, whereas its penetration scale is much less during the low-energy phase. Since the low-frequency variability was absent when there is no DWBC in the second layer, Spall (1996b) concluded that the decadal oscillations in his model simulations were caused by interactions of the Gulf Stream and the upper DWBC. He described the mechanism of the low-frequency variability in terms of wave–mean flow interactions.

However, as Spall (1996b) already noted, it is surprising that similar high-and low-energy states and patterns of low-frequency variability were found in a purely wind-driven homogeneous model by McCalpin and Haidvogel (1996). More recently, Berloff and McWilliams (1999) and Meacham (2000) found low-frequency variability in 1.5- and 2-layer models of wind-driven double-gyre flows as well. These oscillations are also characterized by high-and low-energy states, associated with changes in the zonal penetration scale of the Gulf Stream. The similarities in the low-frequency variability simulated by McCalpin and Haidvogel (1996) and Spall (1996b) illustrate that it is difficult to extract the responsible physical mechanism just from the dominant spatial patterns of the variability. Recent work by Qiu (2000) showed that large-scale interannual changes of the Kuroshio Extension system are also characterized by an oscillation between an elongated and a contracted state. It should be noted that the seven year TOPEX/Poseidon dataset that he analyzed is fairly short to be able resolve these interannual timescales properly. Nonetheless, it is noteworthy that observations indicate that this type of low-frequency behavior, characterized by changes in the penetration scale of the midlatitude jet, is not only occurring in numerical simulations.

In this paper, we focus on the dynamics of the flow in the Gulf Stream/DWBC crossover region. To understand the role of the DWBC in low-frequency variability, we continue a line of studies addressing the stability and variability of wind-driven midlatitude gyres, using techniques of dynamical systems theory (e.g., Jiang et al. 1995; Speich et al. 1995; Dijkstra and Katsman 1997; Berloff and Meacham 1998; Schmeits and Dijkstra 2000). In most of these studies, the transition from simple flows to complex, more realistic, flows is investigated using the magnitude of the lateral friction as a control parameter. At high lateral friction, stationary flows exist with, as a limiting (linear) case, the Sverdrup–Munk flows (Pedlosky 1987). When friction is decreased, these stationary flows lose stability through Hopf bifurcations, which introduce temporal variability with a preferred timescale and pattern. It appears that these timescales are intermonthly for purely wind-driven flows modeled by 2-layer quasigeostrophic theory (Dijkstra and Katsman 1997). At lower friction, subsequent instabilities and nonlinear interactions appear to induce low-frequency variability, as is shown in the studies by McCalpin and Haidvogel (1996) and Berloff and McWilliams (1999).

In this paper, we investigate how this picture of the variability of the wind-driven gyres changes when a DWBC is allowed to dynamically interact with the upper-layer flow. A priori, there seem to be several possibilities depending on whether and how the DWBC (i) modifies the structure of stationary solutions, (ii) changes the preferred timescales arising from instabilities on these stationary solutions, and (iii) modifies the nonlinear interactions in the low-friction regime. In this paper, these issues are systematically studied within a 2-layer quasigeostrophic model in a square basin. The upper-layer flow is wind-driven, while the DWBC is modeled through in- and outflow conditions in the lower layer, which determine its volume transport. Although this setup seems highly idealized, for the purely wind-driven flows the type of variability found in such a simple model was shown to display many qualitative features of the internal variability in cases with realistic geometry and wind forcing (Dijkstra and Molemaker 1999).

In section 2, the approach and numerical model are briefly introduced, with emphasis on the implementation of the DWBC. The stationary solutions for the coupled wind-driven/DWBC system are presented in section 3, for changing values of the lateral friction coefficient. One of the main results is that multiple equilibria disappear under ''realistic'' DWBC strength: only one branch of stationary solutions remains. Stationary solutions on this unique branch are susceptible to instabilities with an intermonthly to interannual timescale. The precise changes in the bifurcation diagram and the changes in the character of the instabilities are investigated in sections 4 and 5, respectively, by gradually

TABLE 1. Dimensional and nondimensional parameters for the 2-layer model.

$f_0 = 1.0 \times 10^{-4}$ s^{-1}	$\beta_0 = 1.6 \times 10^{-11}$ (ms)$^{-1}$	$\tau_0 = 1.5 \times 10^{-1}$ N m^{-2}
$L = 1.0 \times 10^{6}$ m	$D_1 = 0.6 \times 10^{3}$ m	$\rho = 1.0 \times 10^{3}$ kg m^{-3}
$U = 1.6 \times 10^{-2}$ m s^{-1}	$D_2 = 1.4 \times 10^{3}$ m	$g' = 2.0 \times 10^{-2}$ m s^{-2}
$\alpha_\tau = 1.0 \times 10^{3}$	$F_1 = 8.5 \times 10^{2}$	$V_{in} = 2.1$
$\beta = 1.0 \times 10^{3}$	$F_2 = 3.5 \times 10^{2}$	$l = 1.5 \times 10^{-1}$

increasing the strength of the DWBC from zero. In section 6, the time-dependent behavior of the flow is analyzed, both in the presence and the absence of a DWBC, in the low friction regime. The results are summarized and discussed in section 7 and lead to the conclusion that interaction of the Gulf Stream and the DWBC induces a preference for variability on specific interannual timescales.

2. Model formulation and implementation

The 2-layer quasigeostrophic model on a β plane as used in Dijkstra and Katsman (1997) is extended here to allow for a DWBC in the lower layer. The computational domain is a square ocean basin of horizontal dimensions $L \times L = 1000$ km $\times$ 1000 km and of constant depth $D = 2$ km. The two layers have mean thicknesses D_1 and D_2 ($D = D_1 + D_2$) and densities $\rho + \Delta\rho$, respectively. The quasigeostrophic vorticity equations describing the flow are nondimensionalized using characteristic horizontal and vertical length scales L and D, a horizontal velocity scale U, a wind stress scale τ_0, and a timescale L/U, and become (following Pedlosky 1987)

$$\left[\frac{\partial}{\partial t} + u_1\frac{\partial}{\partial x} + v_1\frac{\partial}{\partial y}\right][\zeta_1 - F_1(\psi_1 - \psi_2) + \beta y] = \frac{1}{\mathrm{Re}}\nabla^2\zeta_1 + \alpha_\tau\left(\frac{\partial \tau^y}{\partial x} - \frac{\partial \tau^x}{\partial y}\right) \quad (1a)$$

$$\zeta_1 = \nabla^2\psi_1 \quad (1b)$$

$$\left[\frac{\partial}{\partial t} + u_2\frac{\partial}{\partial x} + v_2\frac{\partial}{\partial y}\right][\zeta_2 + F_2(\psi_1 - \psi_2) + \beta y] = \frac{1}{\mathrm{Re}}\nabla^2\zeta_2 \quad (1c)$$

$$\zeta_2 = \nabla^2\psi_2. \quad (1d)$$

In these equations, the streamfunction ψ_n and vorticity ζ_n are used ($n = 1, 2$), and $(u_n, v_n) = (-\partial\psi_n/\partial y, \partial\psi_n/\partial x)$. The applied wind stress forcing is purely zonal and provides a double-gyre flow in the upper layer:

$$\tau^x(y) = -\frac{1}{2\pi}\cos(2\pi y); \qquad \tau^y = 0. \quad (2)$$

Dissipation is through lateral friction only, and there is no interfacial friction between the two layers. The physical parameters in the equations are the Reynolds number Re, the planetary vorticity gradient β, the wind stress forcing α_τ, and the rotational Froude numbers for the first and second layers (F_1 and F_2). These are given by

$$\mathrm{Re} = \frac{UL}{A_H}; \qquad \beta = \frac{\beta_0 L^2}{U}; \qquad \alpha_\tau = \frac{\tau_0 L}{\rho D_1 U^2};$$
$$F_1 = \frac{f_0^2 L^2}{g' D_1}; \qquad F_2 = \frac{f_0^2 L^2}{g' D_2}, \quad (3)$$

where f_0 is the Coriolis parameter, β_0 is the planetary vorticity gradient, $g' = g\Delta\rho/\rho$ is the reduced gravity, and A_H is the lateral friction coefficient. Standard parameter values used in this study are the same as in Dijkstra and Katsman (1997), and given in Table 1.

To allow for a DWBC in the model, an inflow is prescribed in the northwestern part of the basin, whereas the outflow is over the full width of the southern boundary. In Fig. 1, a plan view of the second layer is shown, together with the applied boundary conditions. The inflow is prescribed over a dimensionless width l ($l < 1$), by defining the streamfunction ψ_2 at the northern boundary as

$$\psi_2 = \begin{cases} -V_{in}x & \text{for } x \in [0, l] \\ -V_{in}l & \text{for } x \in [l, 1] \end{cases} \quad \text{at } y = 1.$$

The (positive) parameter V_{in} controls the strength of the DWBC in the northwest. The value used for l is 0.15, corresponding to a dimensional inflow width of 150 km for the standard model parameters. The dimensional inflow velocity V_{in}^* (m s^{-1}) and the DWBC transport Γ_2^* (m^3 s^{-1}) are

$$V_{in}^* = V_{in}\,U; \qquad \Gamma_2^* = V_{in}UlLD_2.$$

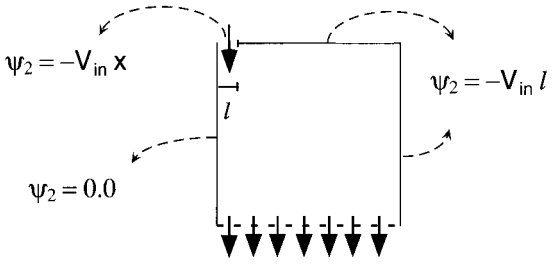

FIG. 1. Plan view of the boundary conditions in the second layer: V_{in} is a control parameter defining the (dimensionless) inflow velocity of the DWBC in the northwest of the basin, over the (dimensionless) width l. The dimensional transport Γ_2^* is defined as $\Gamma_2^* = V_{in}UlLD_2$.

TABLE 2. Overview of the applied boundary conditions for the 2-layer model.

Upper layer	North	free slip	$\psi_1 = 0$	$\zeta_1 = 0$
	South	free slip	$\psi_1 = 0$	$\zeta_1 = 0$
	East	no slip	$\psi_1 = 0$	$\partial\psi_1/\partial x = 0$
	West	no slip	$\psi_1 = 0$	$\partial\psi_1/\partial x = 0$
Lower layer	North	inflow	Condition (4)	$\zeta_2 = 0$
	South	outflow	$\partial\psi_2/\partial y = 0$	$\partial\zeta_2/\partial y = 0$
	East	no slip	$\psi_2 = -V_{\text{in}}l$	$\partial\zeta_2/\partial x = 0$
	West	no slip	$\psi_2 = 0$	$\partial\zeta_2/\partial x = 0$

At the southern boundary, the net outward transport through the boundary is required to amount to the transport coming in through the northern boundary. Therefore, the integrals of the meridional velocity $v_2 = \partial\psi_2/\partial x$ over the open northern and southern boundaries must equal:

$$\int_0^1 \left.\frac{\partial\psi_2}{\partial x}\right|_{y=1} dx = \int_0^1 \left.\frac{\partial\psi_2}{\partial x}\right|_{y=0} dx.$$

Since ψ_2 has to be continuous along each boundary, it is clear from Fig. 1 that this condition is satisfied by prescribing $\psi_2 = 0$ at the western boundary and $\psi_2 = -V_{\text{in}}\, l$ at the eastern boundary. Furthermore, it is required that in the south the flow is normal to the boundary:

$$\frac{\partial\psi_2}{\partial y} = 0; \qquad \frac{\partial\zeta_2}{\partial y} = 0 \quad \text{at } y = 0.$$

In this way, the outflow profile at the southern boundary is not fixed, but can adjust to variations of V_{in} and other model parameters. With these boundary conditions, it is possible that locally the transport through the southern boundary is inward, as long as it is compensated by an outflow elsewhere along this boundary. In practice, this feature has proven not to cause any problems. For the closed boundaries, no-slip conditions are prescribed in the east and west, and free-slip conditions in the north and south, as for the standard model configuration. In Table 2, an overview of all the boundary conditions is given.

The set of equations (1) and the boundary conditions are discretized on a nonequidistant grid of 49 × 33 points. The grid size varies between 3 and 43 km zonally and between 27 and 35 km in the meridional direction, and is smallest near the western boundary and around the central latitude of the basin. A resolution study showed that sufficiently accurate results are obtained with this stretched grid (Dijkstra and Katsman 1997). Using an iterative method, we directly solve the stationary form of the set of equations (1) to find stationary flows for a specific parameter setting. With the help of a continuation algorithm, branches of stationary solutions can be followed as one of the model parameters is varied. In this study, both Re and V_{in} are used as control parameters.

Subsequently, the stability of the stationary solutions along a branch is determined by performing a linear stability analysis. It is assumed that the stationary solution is perturbed by infinitesimally small perturbations φ of the form

$$\varphi(x, y, t) = \hat{\varphi}(x, y)\, e^{\sigma t} = \hat{\varphi}(x, y)\, e^{(\lambda + i\nu)t}.$$

The points in parameter space where the growth rate λ of a specific mode φ changes sign are called bifurcation points. These are of particular interest since they mark a qualitative change in the behavior of the flow. These growth rates can be determined from the (discretized) linear stability problem. The exponents σ are the eigenvalues of the stability problem, while the associated eigenvectors determine the spatial patterns $\hat{\varphi}$ of the modes. Solving the complete discretized linear stability problem is practically impossible for a large-dimensional system. However, to determine the initial destabilization of the flow, only the first few modes (i.e., only the most unstable modes) need to be calculated [see Dijkstra et al. (1995) for details on the numerical implementation].

Examples of bifurcations that can be encountered when one control parameter is changed are limit points, pitchfork bifurcations, and Hopf bifurcations (e.g., Nayfeh and Balachandran 1995). The first two mark a change in the number of stationary solutions that exist for a specific parameter setting, whereas at a Hopf bifurcation point time-dependent behavior is introduced. There, the real part λ of a complex conjugated pair of eigenvalues $\sigma_{1,2} = \lambda \pm i\nu$ changes sign so that the stationary solution becomes unstable to an oscillatory mode φ. Above critical conditions ($\lambda > 0$), the time-dependent behavior of the mode φ is described by

$$\varphi(x, y, t) = [\mathbf{a}_1(x, y)\cos(\nu t) - \mathbf{a}_2(x, y)\sin(\nu t)]e^{\lambda t}. \quad (6)$$

The imaginary part ν of the eigenvalue determines the frequency of the oscillation (the period $p = 2\pi/\nu$), and the two associated eigenvectors, $\mathbf{a}_1$ and $\mathbf{a}_2$, determine the spatial pattern of the mode. Equation (6) only describes the initial growth of the oscillatory mode. As it grows, the assumption that the amplitude of φ is infinitesimally small, used in the linear stability analysis, is no longer valid. Nonlinear processes have to be taken into account to determine the finite amplitude evolution of the mode.

A nice spin-off of stationary state-solvers is the immediate availability of a second-order accurate implicit time-integration scheme. Such a time-dependent version of the 2-layer quasigeostrophic model is applied to calculate transient purely wind-driven and coupled wind-driven/DWBC flows in section 6. The trajectories are initialized with the known stationary solution for the specific parameter setting, and perturbed with the most unstable mode known from the linear stability analysis. This method assures a fast deviation of the time-dependent flow away from this stationary solution.

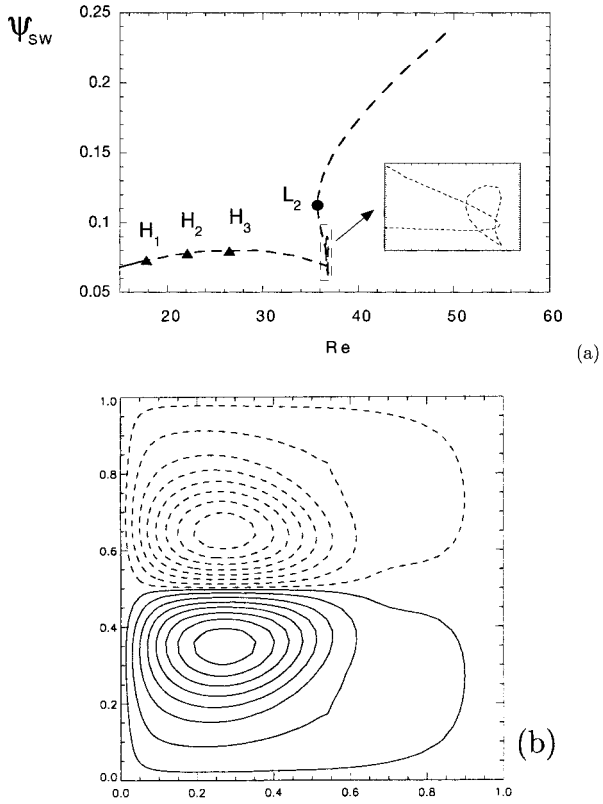

FIG. 2. (a) Bifurcation diagram for the purely wind-driven double-gyre flow ($\Gamma_2^* = 0.0$), as a function of Re. On the vertical axis, ψ_1 at a grid point in the southwest of the domain [at $(x, y) = (0.02, 0.14)$] is plotted as the measure ψ_{SW} of the stationary solutions. Solid (dashed) lines indicate (un-) stable solution branches. Marked are three Hopf bifurcations H_1, H_2, and H_3 (triangles) and a limit point (L_2). The inset shows the multiple solutions between Re = 36 and Re = 37. (b) Contour plot of the upper-layer stationary solution at Re = 31 (contour interval is 0.3; the lower layer is motionless).

3. Impact of the presence of a DWBC

As ''realistic'' strength of the DWBC, a transport of 7.2 Sv is chosen, which corresponds to $V_{in} = 2.1$ or $V_{in}^* = 3.4$ cm s^{-1}. In this section, the stationary solutions and the stability characteristics of the wind-driven flow obtained when such a DWBC is present are contrasted with those obtained when such a DWBC is absent.

The latter results were computed for $\Gamma_2^* = 0$ and closed lateral boundaries in Dijkstra and Katsman (1997), and are recapitulated here shortly. In Fig. 2a, the bifurcation diagram for this purely wind-driven flow is shown. In this diagram, the stationary solutions for the flow are presented as a function of the Reynolds number Re, which serves as the control parameter. On the vertical axis, a particular measure of the stationary solutions is plotted. Here, we use the value of the upper-layer streamfunction ψ_1 at a grid point in the southwest of the domain [at $(x, y) = (0.02, 0.14)$] to represent the flow. This measure is indicated as ψ_{SW}. Solid (dashed) branches indicate linearly (un)stable solutions and bifurcation points are indicated by markers. There is no flow in the second layer for any of the stationary solutions for the purely wind-driven flow ($\psi_2 = 0$) since the wind stress forcing only acts on the upper layer and interfacial friction is not incorporated in the model. For a stationary solution, the lower layer is therefore unforced and hence motionless (Pedlosky 1996). Despite that $\psi_2 = 0$, the second layer is of importance for the stability of the wind-driven flows, as was shown in Dijkstra and Katsman (1997).

For low values of Re, the stationary solution is unique, and ψ_1 is perfectly antisymmetric with respect to the midaxis of the basin as a result of the symmetry properties of the quasigeostrophic model (see Dijkstra and Katsman 1997). Since the zonal velocity of the solutions on this branch is symmetric, the branch will be referred to as the symmetric branch. The circulation is still relatively weak (ψ_{SW} is small) and the flow is linearly stable (solid line on the left in Fig. 2a). As *Re* is increased, the circulation becomes stronger (ψ_{SW} increases) and becomes susceptible to baroclinic instabilities. Three oscillatory modes with intermonthly timescales destabilize the flow at the Hopf bifurcations marked H_1, H_2, and H_3 in Fig. 2a [for details, see Dijkstra and Katsman (1997)]. The symmetric, unstable stationary solution for Re = 31 is shown in Fig. 2b. Between Re = 35.7 and Re = 36.9, multiple symmetric equilibria exist due to the existence of two limit points (only the second limit point L_2 is marked explicitly in Fig. 2a). Moreover, a small interval in Re exists where multiple asymmetric equilibria are found (inset in Fig. 2a). These asymmetric solutions appear through symmetry-breaking pitchfork bifurcations, and both solutions with a stronger (weaker) subpolar and a weaker (stronger) subtropical gyre exist.

Such a bifurcation diagram is also constructed for the coupled wind-driven/DWBC flow. The DWBC transport is set at $\Gamma_2^* = 7.2$ Sv, while all other parameters are kept the same as for the purely wind-driven flow. In Fig. 3a, the stationary solution branches are plotted with again Re on the horizontal axis, and the same measure for the solution on the vertical axis. For comparison, the solutions found for the purely wind-driven flow are shown in Fig. 3a as dotted curves. With a DWBC of the chosen strength, only one branch of solutions is found for the investigated range in Re [Re $\in$ (20, 125)]. The flow first becomes unstable through a Hopf bifurcation marked $\mathcal{H}_1$ in Fig. 3a, at Re = 25.8. At this Hopf bifurcation, the growth rate of a particular oscillatory mode becomes positive. However, at Re = 29.7 the growth rate of this mode becomes negative again, and the flow stabilizes through a reverse Hopf bifurcation (not explicitly marked in Fig. 3a, but visible as the transition from a dashed to a solid branch).

A stability analysis of the stationary solutions reveals that for Re $\in$ (20, 125) nine different modes destabilize the flow. The timescales of these modes [which will be referred to as B_1 to B_9 (*B* for boundary current)] vary from 0.7 to 22.3 years at critical conditions. In Fig. 3a,

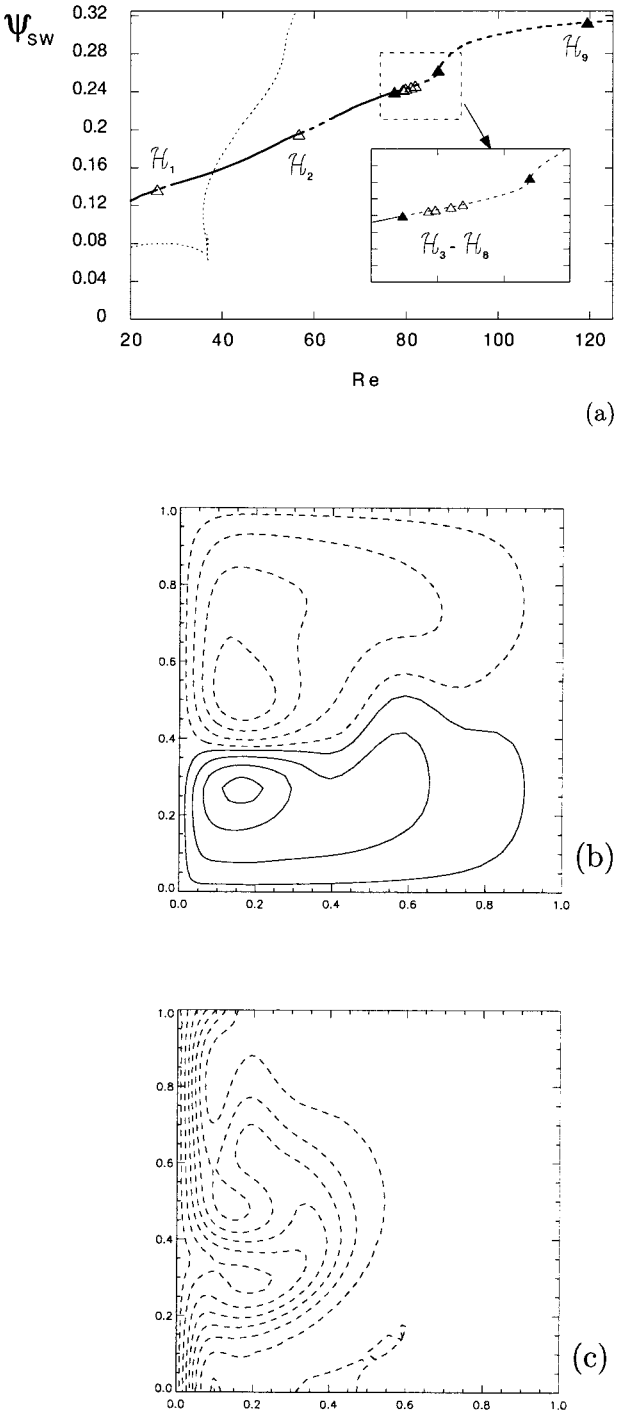

FIG. 3. (a) Bifurcation diagram for the coupled wind-driven/DWBC flow ($\Gamma_2^* = 7.2$ Sv), as a function of Re. The same measure ψ_{SW} as used in Fig. 2a is plotted on the vertical axis. For comparison, the solution branches for the purely wind-driven flow that were shown in Fig. 2a are indicated here by a dotted line. Marked are the Hopf bifurcation points $\mathcal{H}_1$–$\mathcal{H}_9$ (triangles). Solid triangles are used when the associated modes remain unstable for increasing Re, and open triangles for the bifurcation points associated with those modes that stabilize again through a reverse Hopf bifurcation. [(b)–(c)] Contour plot of the stationary solution at $Re = 31$, in the upper and lower layers. Contour interval is 0.3 in (b) and 0.05 in (c).

the Hopf bifurcation points where the modes become unstable are marked $\mathcal{H}_1$ to $\mathcal{H}_9$. Six of the oscillatory modes (including B_1) stabilize again for larger values of Re through a reverse Hopf bifurcation, but three of them remain unstable. Hopf bifurcations associated with the latter modes are marked with solid triangles in Fig. 3a, the others with open triangles. The modes that stabilize again attain maximum dimensional growth rates $\lambda^* = \lambda U/L$ of 0.04–1.0 yr^{-1}.

The linearly stable stationary flow at Re = 31 is plotted in Figs. 3b–c. The upper-layer jet flows northeastward, and its separation point lies 125 km south of the zero wind stress curl line (the midaxis of the basin). This is in contrast to the symmetric wind-driven flows (Fig. 2b), for which separation occurs exactly at the midaxis of the basin. In the second layer, the DWBC mainly follows the western boundary southward, until it reaches the crossover region where it is deflected (north) eastward. It returns to the coast farther south and then continues along the western boundary again. Despite the obvious simplifications of our model setup, the stationary solutions show basic features of the Gulf Stream/DWBC interaction simulated by more complicated models. As in Thompson and Schmitz (1989), the separation point shifts southward due to the presence of the DWBC (Figs. 3b,c). The deflection of the DWBC near the crossover point is also captured by the model.

When Figs. 2 and 3 are compared, it is clear that the presence of the DWBC has a large impact on the structure of the bifurcation diagram, on the spatial patterns of the stationary solutions, and on their stability characteristics. First, when the DWBC is present regimes of multiple equilibria do not exist. The precise details of this transition towards unique stationary flows is explored in section 4. Second, whereas only intermonthly oscillatory modes destabilize the flow in absence of a DWBC, interannual to decadal modes destabilize the flow when a DWBC is present. The preference of the coupled wind-driven/DWBC flow for these longer timescale instabilities is investigated in section 5.

4. Stationary solutions

The multiple stationary equilibria found for the purely wind-driven flow have disappeared when a DWBC of 7.2 Sv is present (Figs. 2a and 3a). By gradually increasing the strength of the DWBC from zero, the results of the two cases can be connected and the fate of the multiple equilibria can be studied.

A detail of the bifurcation diagram for the wind-driven flow ($\Gamma_2^* = 0.0$) is shown as dotted lines in Fig. 4a, showing (part of) the region where multiple equilibria exist [the interval $Re \in (36.5, 37.0)$]. Three limit points (L_1, L_{3a}, and L_{3b}) and two pitchfork bifurcations (P_1 and P_2) are marked in this figure. The limit point L_2 (shown in Fig. 2a) lies outside the range in Re displayed here. The symmetric solution branch is marked "S," while asymmetric solutions branching off at pitchfork bifur-

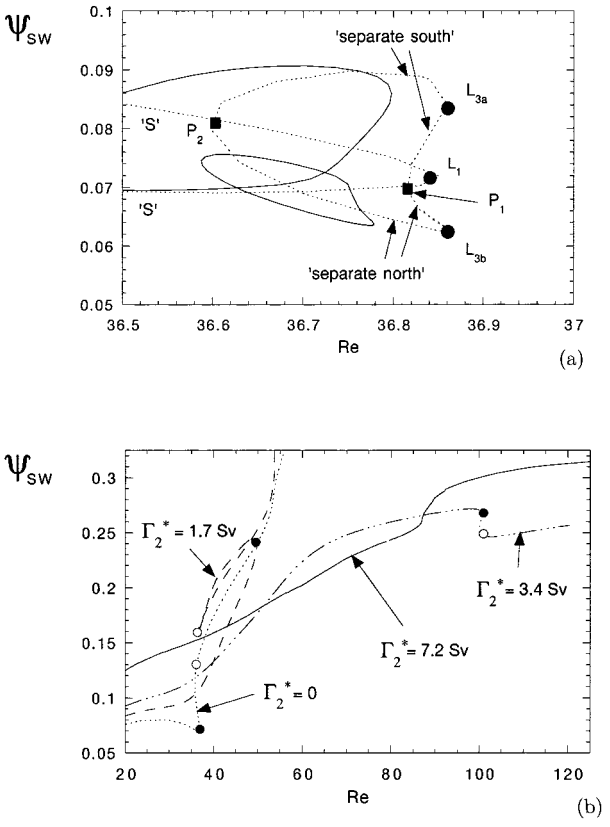

FIG. 4. Bifurcation diagrams as a function of Re, for varying strengths of the DWBC. (a) Detail between Re = 36.5 and 37.0, for $\Gamma_2^* = 0.0$ (dashed) and $\Gamma_2^* = 0.003$ Sv (solid); (b) bifurcation diagram between Re = 20 and 125, for $\Gamma_2^* = 0.0$, 1.7, 3.4, and 7.2 Sv (dotted, dashed, dash-dotted, and solid branches, respectively). The limit points L_2 and L_{3a} are marked in (b) by open and filled circles.

cations are marked ''separate south'' and ''separate north,'' indicating that the upper-layer jet separates south or north of the midaxis of the basin, respectively. The solutions with a southerly (northerly) separation have a stronger subtropical (subpolar) gyre, so ψ_{SW} is larger (smaller).

In Fig. 4a, the solution branches for $\Gamma_2^* = 0.003$ Sv are plotted as well (solid lines). The presence of this weak DWBC destroys the reflection symmetry of the system around the midbasin. Hence, the pitchfork bifurcations that mark the spontaneous breaking of the internal symmetry of the solutions for the purely wind-driven flow no longer exist. The former symmetric solution branch now connects to the solution branch with the stronger subtropical gyre (''separate south''). The two asymmetric solution branches with a stronger subpolar gyre (''separate north'') form a closed loop. This loop shrinks when Γ_2^* is increased further, and ultimately vanishes. So, the stationary solutions with a jet separating north of the midaxis of the basin cannot exist in the presence of a DWBC, and only a branch of solutions with a jet that separates south of $y = 0.5$ remains. This is consistent with findings by Thompson and Schmitz (1989) and Tansley and Marshall (2000), that the DWBC pushes the separation point southward.

Despite the disappearance of the separate north branch, multiple stationary solutions still exist when the DWBC transport is weak, due to the limit points L_{3a} and L_2. However, when the DWBC transport Γ_2^* is increased further, these limit points on the separate south branch disappear as well. To show this, in Fig. 4b the remaining stationary solution branch is plotted as a function of Re for various DWBC transports. For a DWBC transport $\Gamma_2^* = 1.7$ Sv, L_{3a} (marked by a filled circle in Fig. 4b) has moved to a larger value of *Re* while L_2 (open circle) remains in the same position. For $\Gamma_2^* = 3.4$ Sv, the limit points are found closer together and have both moved to higher values of Re ($\mathrm{Re}_{L_{3a}} = 100.7$ and $\mathrm{Re}_{L_2} = 100.2$). Finally, when the DWBC is strong enough, multiple equilibria do not exist anymore; no limit points are found for Re up to 125 for $\Gamma_2^* = 7.2$ Sv. So, the regimes of multiple equilibria that were found for purely the wind-driven flow are no longer present when a DWBC is introduced.

As the strength of the DWBC is increased, the spatial patterns of the stationary solutions change significantly. For $\Gamma_2^* = 0.0$, the stationary solution at Re = 31 is symmetric (see Fig. 2b). For a weak DWBC, the symmetric solution branch connects to the separate south branch (Fig. 4a), and hence one expects a stationary solution with a jet that separates south of the midaxis of the basin. Examples of stationary flows for increasing Γ_2^* and Re = 31 are shown in Fig. 5. For $\Gamma_2^* = 1.7$ Sv (Figs. 5a,b), the jet indeed separates slightly south of $y = 0.5$. The jet direction changes to northeastward for increasing DWBC transports, and stationary meanders develop. The separation point of the upper-layer jet shifts southward with increasing Γ_2^*, as in Thompson and Schmitz (1989). It shifts over a distance of 35 km for $\Gamma_2^* = 1.7$ Sv and over 250 km for $\Gamma_2^* = 10.0$ Sv. In the second layer, the undercurrent follows the coastline until it reaches the crossover region. There, part of the flow continues along the coast and part gets deflected eastward and crosses the midlatitude jet east of the recirculation cells in the upper layer. For higher transports, the DWBC is deflected less far into the basin in the crossover region. As is clear from Fig. 5e, a DWBC transport of 10 Sv induces a southward shift of the separation point, which is very large compared to the basin size of 1000 *km*. The interaction between the wind-driven gyres and the DWBC is quite vigorous as a consequence of the relatively shallow layer depths chosen here. To allow for a fair comparison with the results presented in Dijkstra and Katsman (1997), we kept the layer depths the same as in that study and used a weaker transport of 7.2 Sv as the standard value.

For a purely wind-driven flow a southerly separation is associated with a stronger subtropical gyre. However, for $\Gamma_2^* = 1.7$ Sv, the subpolar gyre of the solution is stronger than the subtropical gyre (Fig. 5a). This strengthening of the subpolar gyre can be explained by

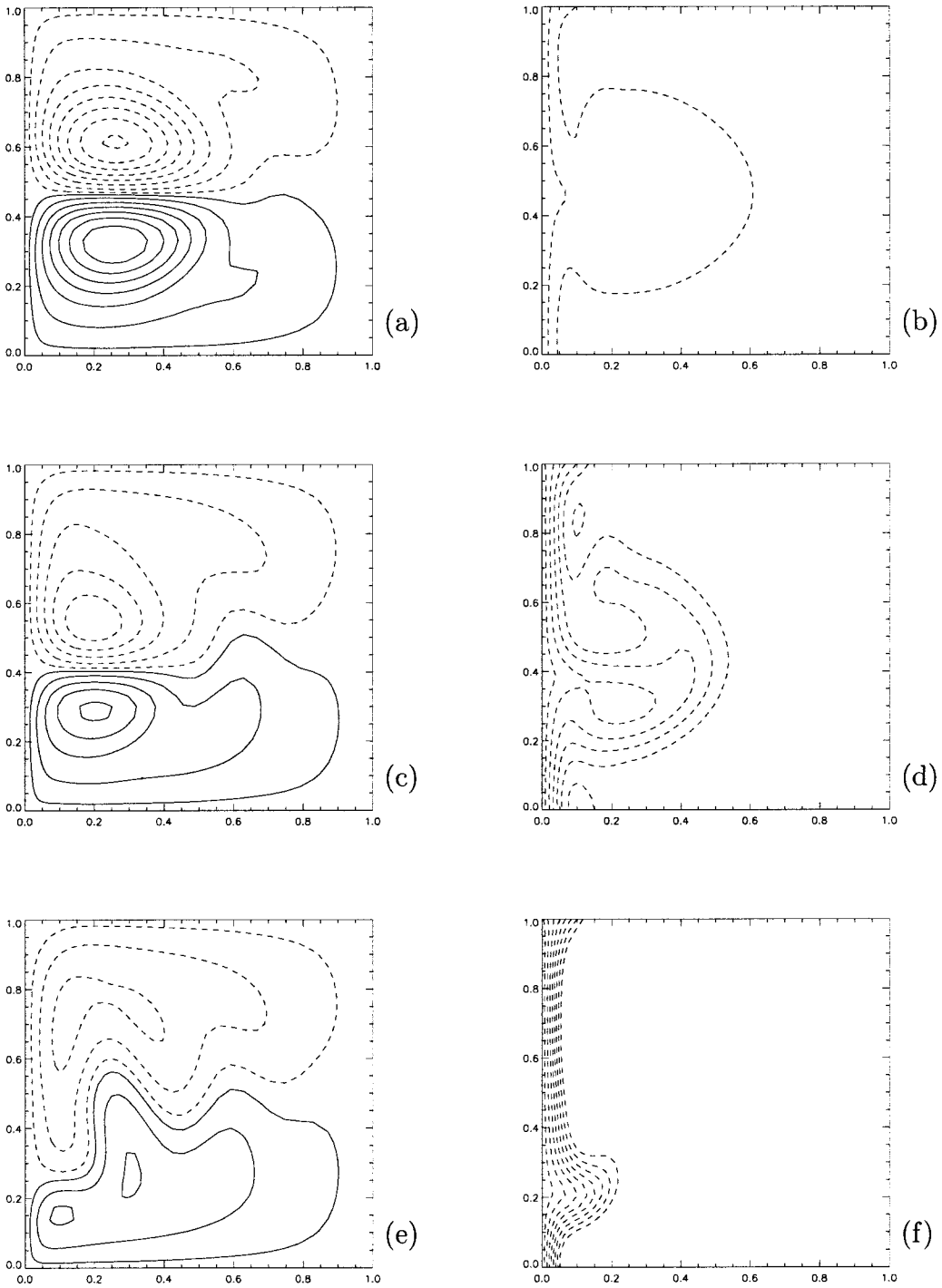

FIG. 5. Streamfunction of the stationary solution in the (left) upper and (right) lower layers for a fixed Reynolds number (Re = 31) and [(a)–(b)] $\Gamma_2^* = 1.7$ Sv, [(c)–(d)] $\Gamma_2^* = 5.0$ Sv, and [(e)–(f)] $\Gamma_2^* = 10.0$ Sv. Contour interval is 0.3 in the upper and 0.05 in the lower layer. Recall that the stationary solutions for $\Gamma_2^* = 0.0$ and 7.2 Sv were already shown in Figs. 2b, 3b, and 3c, respectively.

considering the conservation of potential vorticity for the coupled wind-driven/DWBC flow. As long as the DWBC is weak, its presence mainly alters the potential vorticity balance through vortex stretching. Since $\psi_2 <$ 0 over the whole domain, the upper-layer depth h_1 (which is proportional to $\psi_1 - \psi_2$) increases. This increase in h_1 tends to reduce the potential vorticity of the flow. To conserve potential vorticity, additional pos-

itive relative vorticity is required, consistent with a stronger subpolar and a weaker subtropical gyre in the upper layer. For higher values of Γ_2^* the maximum of the upper-layer streamfunction reduces but the subpolar gyre remains strongest (Figs. 5c–f).

5. Internal modes of variability

In this section, focus is on the fate of the intermonthly modes found for the wind-driven flow, and on the origin of the low-frequency modes found for the coupled wind-driven/DWBC flow, as presented in section 3.

a. The stabilization of intermonthly modes

In Fig. 6a, the dimensional growth rates $\lambda^* = \lambda U/L$ of the three oscillatory modes that were found to destabilize the symmetric, purely wind-driven flow are plotted against Γ_2^* for a fixed Reynolds number Re = 31. For $\Gamma_2^* = 0$, these modes all have positive growth rates at Re = 31. It appears that increasing the strength of the DWBC strongly damps these three modes, and for $\Gamma_2^* > 5.4$ Sv none of them is able to destabilize the flow anymore. As Γ_2^* is increased, the periods of the modes increase slightly. The stationary solutions become stable with respect to these baroclinic modes as a result of changes in the solutions themselves. While there is a weak DWBC or no inflow at all, well-developed recirculation gyres exist that give rise to a sharp jet (see Fig. 5a). As a consequence, the vertical shear $|\mathbf{u}_1 - \mathbf{u}_2|$ is quite large (up to 40 cm s^{-1}). When the strength of the DWBC is increased, the vertical shear is strongly reduced since the amplitude of ψ_1 decreases and because the DWBC is deflected in the crossover region.

One might expect that the stationary flow can be destabilized again by these baroclinic modes when the vertical shear of the stationary solution increases, for example at larger Re. However, when Re is increased for a fixed value of $\Gamma_2^* = 7.2$ Sv, the coupled wind-driven/DWBC flow remains stable to this type of perturbations with an intermonthly timescale. Hence, the interannual modes found to destabilize the coupled wind-driven/DWBC flow are not simply a modification of these intermonthly modes.

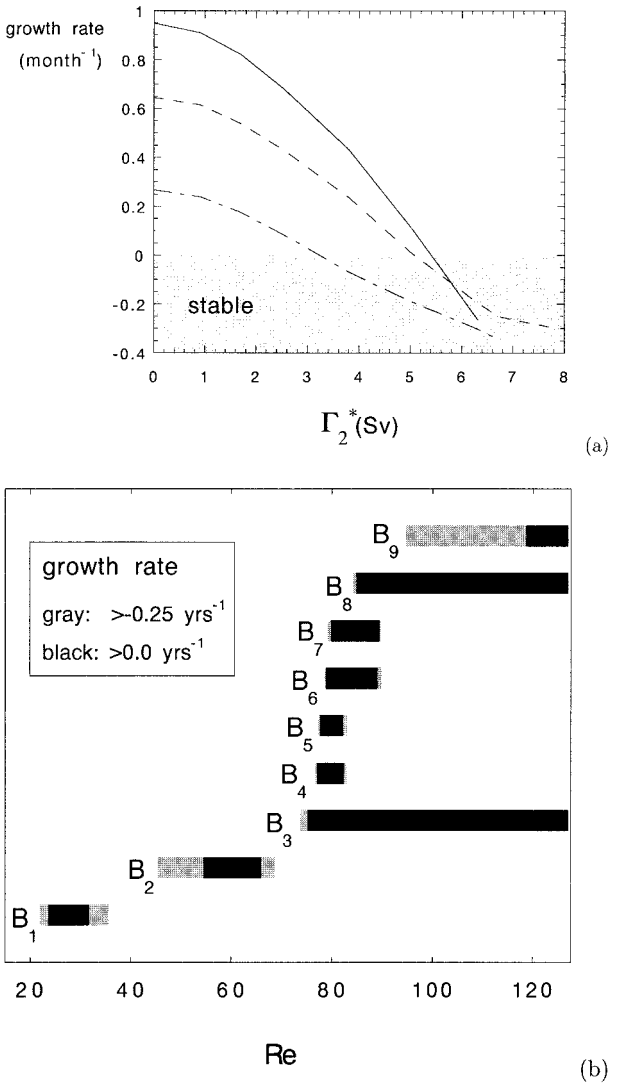

FIG. 6. (a) Dimensional growth rates $\lambda^* = \lambda U/L$ of the modes that destabilize the purely wind-driven flow, for a fixed Reynolds number (Re = 31) and increasing Γ_2^*. Solid, dashed, and dash-dotted lines are used for the growth rate of the modes associated with H_1, H_2, and H_3 in Fig. 2a, respectively. (b) Dimensional growth rates λ^* of the modes B_1–B_9 that destabilize the coupled wind-driven/DWBC flow, associated with the Hopf bifurcations $\mathcal{H}_1$–$\mathcal{H}_9$ in Fig. 3a, for a fixed DWBC transport ($\Gamma_2^* = 7.2$ Sv) and increasing Re. Shown are the intervals in Re where the modes have positive growth rates ($\lambda^* > 0$; black) or are only marginally damped ($\lambda^* > -0.25$ yr^{-1}: gray).

b. The appearance of low-frequency variability

For $\Gamma_2^* = 7.2$ Sv, nine different modes were found to destabilize the coupled wind-driven/DWBC flow (see section 3). In Fig. 6b, the intervals in Re along the branch of stationary solutions in Fig. 3a where each of these nine modes has a positive growth rate ($\lambda^* > 0$: black) or is only marginally damped ($\lambda^* > -0.25$ yr^{-1}: gray) are presented. Six of the oscillatory modes have positive growth rates only over a small interval in Re before they stabilize again through a reverse Hopf bifurcation and, hence, are of lesser importance for the variability. In contrast, the modes B_3, B_8, and B_9 are expected to contribute to the time-dependent behavior of the flow over a larger interval in Re. Only the characteristics of these latter modes are discussed in detail here. Contour plots of the perturbation streamfunction φ of these modes, in both upper and lower layers, are shown in Fig. 7 for one phase of the oscillation ($\nu t = 0.0$). Note that the amplitude of the mode is arbitrary but that the ratio of the amplitude in the upper and lower layers is determined from the linear stability analysis. Hence, for each mode the two fields are scaled with the

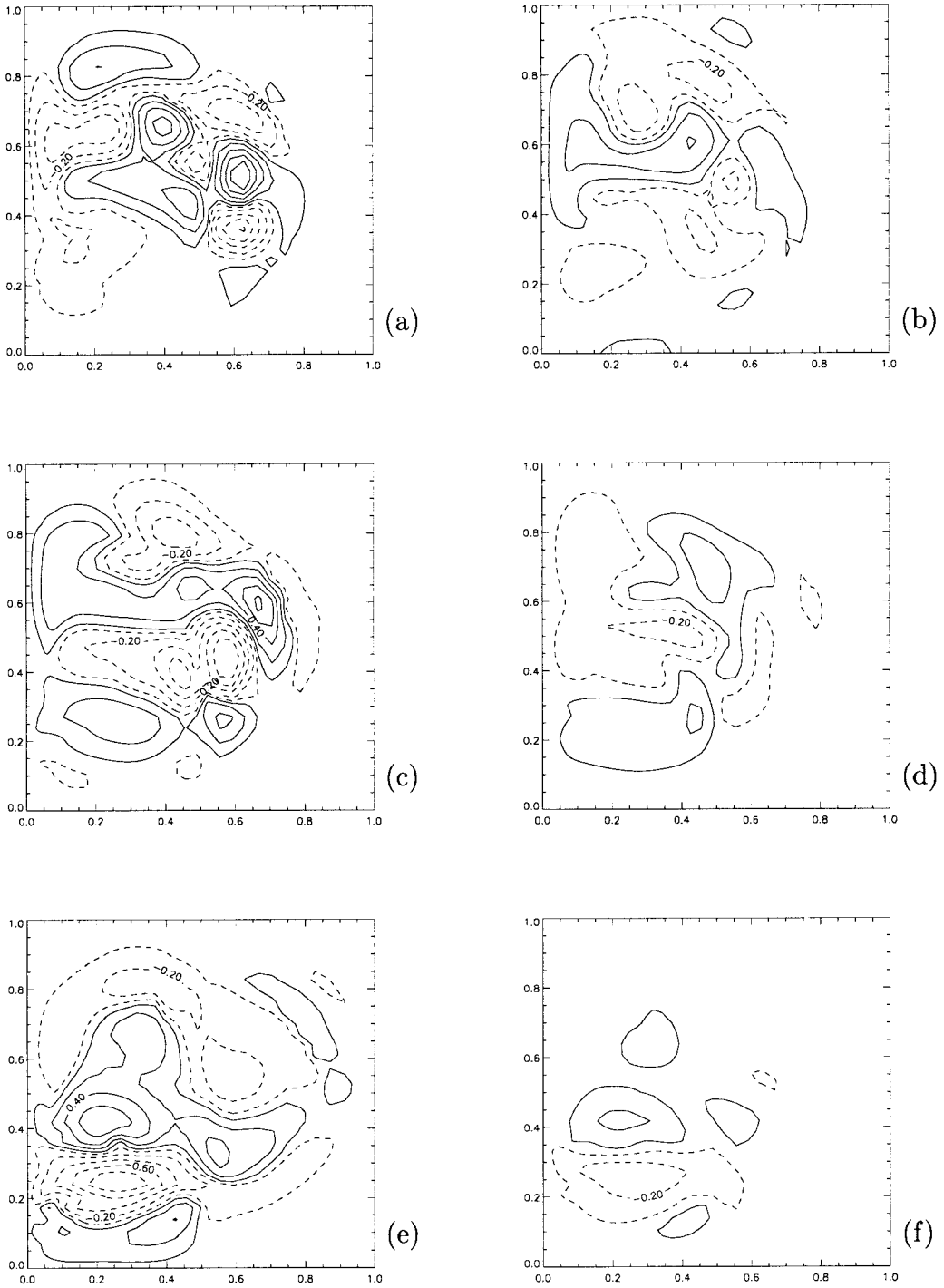

FIG. 7. Snapshots of the modes B_3, B_8, and B_9 in the (left) upper and (right) lower layers at phase $\nu t = 0.0$. [(a)–(b)] B_3 (period $p^* = pL/U = 0.7$ yr at criticality), [(c)–(d)] B_8 ($p^* = 1.4$ yr) and [(e)–(f)] B_9 ($p^* = 5.1$ yr). For each mode, the plots are scaled with the maximum of the perturbation streamfunction ϕ_1 in the upper layer.

maximum of the upper-layer perturbation streamfunction.

At $\mathcal{H}_3$ (Re = 77.4), the stationary flow is destabilized by the mode B_3 (Figs. 7a,b), which has a period of 8.2 months at criticality. Its main features are the $O(150)$ km anomalies in the strip between $(x, y) = (0.4, 0.7)$ and $(x, y) = (0.6, 0.4)$ in both layers. During a cycle, these anomalies propagate southeastward from $(x, y) = (0.4, 0.7)$ toward $(x, y) = (0.6, 0.4)$ where they decay again. A phase difference exists between the response

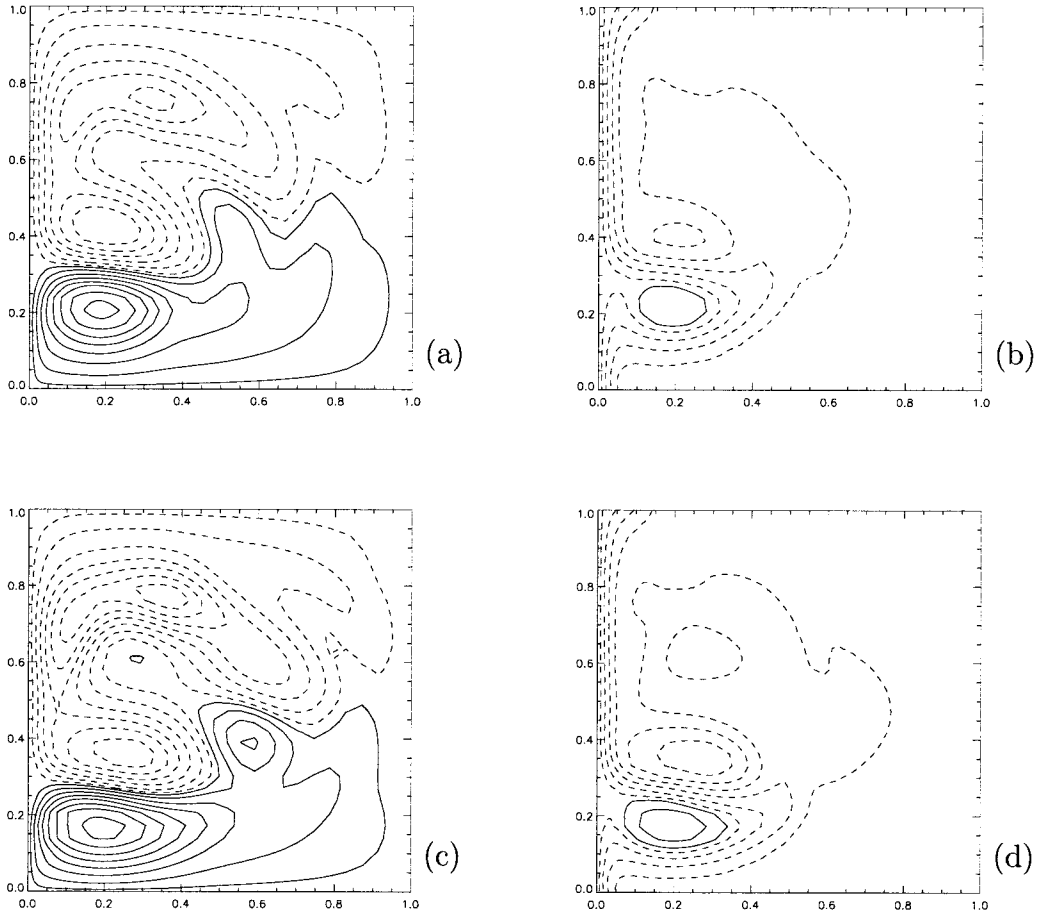

FIG. 8. Spatial patterns of the stationary solution in the (left) upper and (right) lower layers at [(a)–(b)] Re = 78 and [(c)–(d)] Re = 121. Contour interval is 0.2 in the upper layer and 0.05 in the lower layer.

in the two layers: the lower layer leads the upper layer. In Figs. 8a and 8b, the stationary solution at Re = 78, near the bifurcation point $\mathcal{H}_3$, is shown for comparison. The upper-layer jet of the stationary solution has a strong meander in the area where B_3 shows the strongest response, whereas there is only a weak circulation in the lower layer in this region.

At $\mathcal{H}_8$ (Re = 87.0), an oscillatory mode with a timescale of 1.4 yr becomes unstable (B_8; Figs. 7c,d). The stationary solution at this Reynolds number has not changed much compared to that in Figs. 8a and 8b and is therefore not shown. The mode shows a response on somewhat larger spatial scales than B_3, and the strongest anomalies develop near the center of the domain. During the cycle they propagate (north) westward with the return flow of the subpolar gyre (see Figs. 8a,b), and decay near the western boundary around $(x, y) = (0.1, 0.8)$. Again, a phase difference exists between the response in the two layers, with the lower layer leading the upper layer. Both B_3 and B_8 mainly affect the midlatitude jet near the center of the basin.

The third oscillatory mode for which the stationary flow remains unstable for increasing Re has a period of 5.1 yr at criticality (B_9: Figs. 7e,f). This mode destabilizes the flow at the bifurcation point $\mathcal{H}_9$ at Re = 120.8, a Reynolds number which corresponds to a lateral friction coefficient $A_H = 130\ \mathrm{m^2\ s^{-1}}$. It is, based solely on its period, the most interesting mode of variability for comparison with the low-frequency variability found by Spall (1996b). The most important features of the mode are two large-scale anomalies centered at $(x, y) = (0.2, 0.25)$ and $(0.2, 0.4)$ at phase $\nu t = 0.0$. These are aligned with the recirculation gyres of the stationary solution at this Reynolds number, shown in Figs. 8c and 8d. The propagation of these two anomalies during a cycle is visualized in Fig. 9 by two sections through the basin at a fixed latitude as a function of time. In this figure the dimensionless time $\hat{t}$, measured in units of the period $p = 2\pi/\nu$, is plotted on the vertical axis. The zonal coordinate x is on the horizontal axis. The positive anomaly, which at time $\hat{t} = 0.0$ is present in the northern recirculation gyre at $(x, y) = (0.2, 0.4)$, first propagates (south) eastward. Its path is captured in the section through $y = 0.4$ in Fig. 9a, while moving from $(x, \hat{t})$

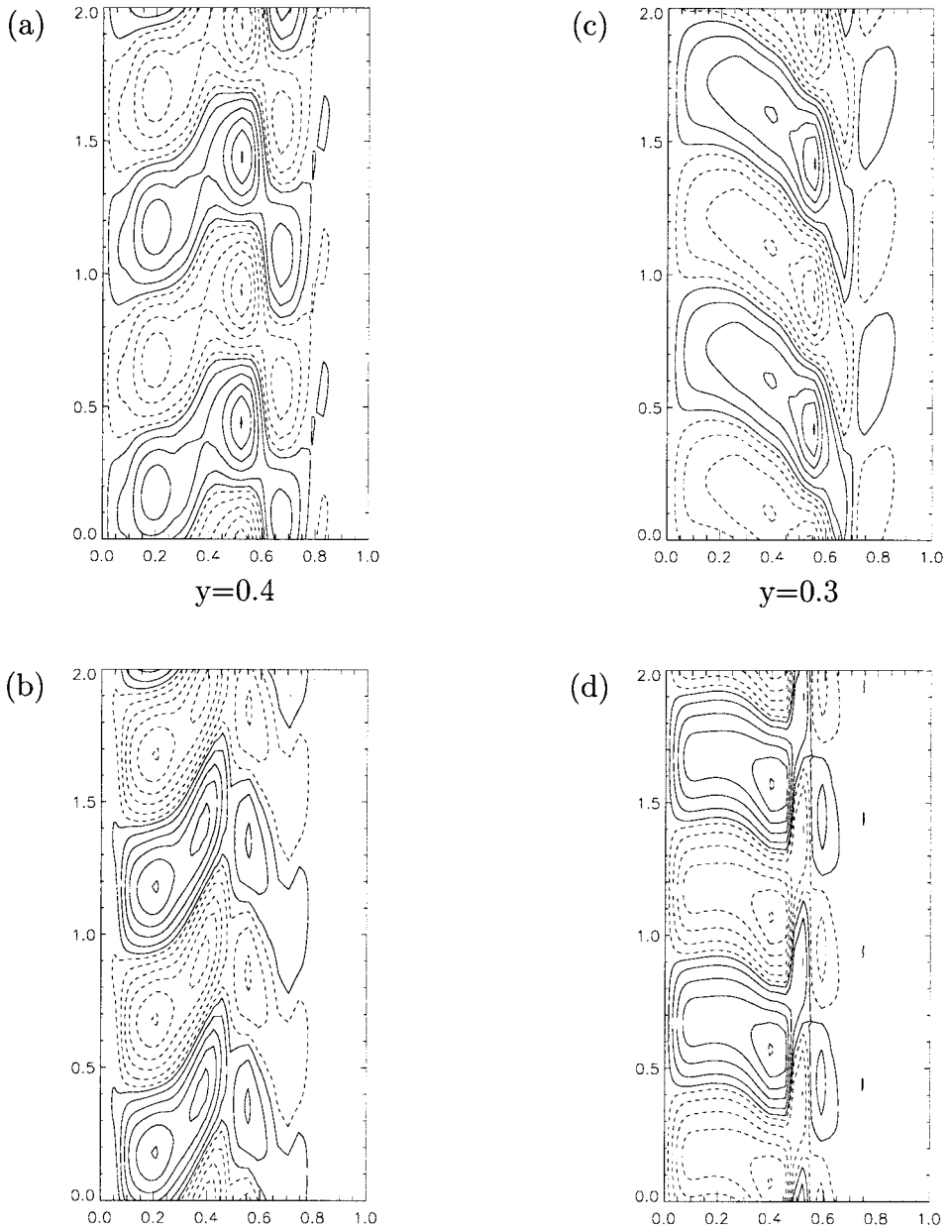

FIG. 9. Longitude–time diagrams displaying the propagation of the mode B_9, by (a–b) a section along $y = 0.4$ and (c–d) a section along $y = 0.3$. Two oscillation periods are shown [$\hat{t} = t/p \in (0, 2)$, $p = 2\pi/\nu$], both for the (top) upper and (bottom) lower layer.

$= (0.2, 0.0)$ towards $(x, \hat{t}) = (0.45, 0.5)$ in the upper layer. In the second layer (Fig. 9b), the propagation of the anomaly is similar. Subsequently, this positive anomaly returns to the western boundary following a (south) westward course. Its path is clearly visible in Figs. 9c and 9d, a section through $y = 0.3$, as it moves from $(x, \hat{t}) = (0.45, 0.5)$ toward $(x, \hat{t}) = (0.2, 0.8)$. A negative anomaly follows the same path as the positive anomaly half a cycle later. This interannual mode has its strongest response in a region where both the surface and the deeper circulation are strong, that is, in the crossover region.

Summarizing the results in this section, we can conclude that the coupled wind-driven/DWBC flow becomes unstable to different modes of variability than the purely wind-driven flow. These new modes have intermonthly to interannual timescales. Furthermore, other perturbations on timescales of years to decades exist that are only marginally damped over large intervals in Re. However, to assess their importance it needs

to be verified that the low-frequency modes discussed in this section indeed contribute substantially to the time-dependent behavior of the flow at low friction. In particular, the contribution of B_9 to the variability is of interest.

6. Transient flows at low friction

Similar to the approach followed by, for example, McCalpin and Haidvogel (1996) and Spall (1996b), transient flows are computed. Here we compare the time-dependent behavior of a purely wind-driven flow to that of a coupled wind-driven/DWBC flow, both at low friction (Re = 130). The parameter setting for these two integrations is the same except for the absence or presence of a DWBC of 7.2 Sv. In both cases, low-frequency variability is expected to arise. Based on the results presented in Dijkstra and Katsman (1997) and in this paper, it is presumed that for the purely wind-driven flow this low-frequency variability will be caused by nonlinear interactions of high-frequency modes, since no low-frequency modes were detected and multiple stationary equilibria were not found to exist for high Re either. In contrast, for the coupled wind-driven/DWBC flow, internal modes on interannual timescales are expected to play a role.

To get an objective measure of the variability in the computed time series for the two cases, a statistical analysis is used to extract both the dominant timescales and the associated spatial patterns of variability [Multivariate Singular Spectrum Analysis (M-SSA): see, e.g., Plaut and Vautard (1994)]. In the analysis, we use both the upper- and lower-layer flow patterns of the last 42 years of the two computed time series, sampled at intervals of one week. Hence, the phase relation between the response in the upper and lower layers is retained, and both high- and low-frequency signals can be distinguished. The timescales and spatial patterns obtained from the M-SSA analysis are inspected visually and compared to the results of the linear stability analysis, to identify the specific internal modes that contribute most to the variability. The same approach was successfully applied to analyze the results of time integrations for the purely wind-driven flow at relatively high friction (Katsman et al. 1998; Dijkstra et al. 1999). In the parameter regime considered in those studies (Re $<$ 60 or $A_H > 270$ m^2 s^{-1}), variability on longer timescales than intermonthly was not found.

For the purely wind-driven flow ($\Gamma_2^* = 0.0$), the time series for ψ_{SW} and for the upper-layer kinetic energy at Re = 130 are shown in Figs. 10a and 10b. The time-dependent behavior is characterized by high-, medium-, and low-energy states, in accordance with the results by McCalpin and Haidvogel (1996), Berloff and McWilliams (1999), and Meacham (2000). Time mean states, averaged over a high- and a low-energy period (years 27–29 and 39–41, respectively), are shown in Figs. 10c to 10f. In line with the studies mentioned above, a high-energy state (low-energy state) is characterized by stronger (weaker) recirculation cells and a larger (smaller) penetration scale of the midlatitude jet. The M-SSA analysis of this time series reveals that the most dominant statistical modes have timescales of 2.0 months, 10 years, 6.7 years and 2.0 months, and explain 20%, 15%, 8%, and 3% of the total variability, respectively. The high-frequency modes are identified as barotropic Rossby basin modes (see Pedlosky 1987). For an inviscid fluid in a closed basin, the Rossby basin modes are the free-mode solutions of the model. They are the equivalent of free Rossby waves in an unbounded ocean, have intermonthly timescales and basinwide spatial patterns, and propagate westward like Rossby waves (Dijkstra et al. 1999). The low-frequency mode with the timescale of 10 yr hardly propagates, and its spatial pattern simply seems to display the difference between the high- and the low-energy states. The low-frequency mode with the timescale of 6.7 yr exhibits similar behavior. Their patterns do not correspond to any of the internal modes that were detected.

For the coupled wind-driven/DWBC flow at Re = 130, the time series for ψ_{SW} is shown in Fig. 11a. During the first few years of the integration, perturbations on the initial state are still very small and, hence, hardly visible. In the remainder of the time series, both high- and low-frequency variability signals are clearly present. Similar behavior is observed in time series of the kinetic energy of the upper layer (Fig. 11b). In Figs. 11c to 11f, the mean states of the flow are shown (averages are over years 16–18 for the high-energy state and over years 38–39 for the low-energy state). Again, the penetration scale of the jet is larger for the high-energy state, and the DWBC is deflected more in the crossover region.

The most dominant statistical mode of variability in the time series shown in Figs. 11a and 11b explains 33% of the total variability. It is an oscillation with a timescale of 4.0 yr. In Fig. 12, a snapshot of the spatial pattern of this statistical mode is shown. It resembles that of the linearly unstable mode B_9 shown in Figs. 7e and 7f: its main features are two anomalies of opposite sign present in both layers, centered at $(x, y) = (0.25, 0.25)$ and $(x, y) = (0.25, 0.45)$. Moreover, the propagation of the mode is similar to that of B_9. Thus, we conclude that 33% of the variability in the time series is due to the linearly unstable mode B_9. Apparently, the timescale of the mode is slightly modified at these supercritical conditions (recall that at criticality, the period of B_9 is 5.1 yr). The second and third most dominant statistical mode are both oscillations with a timescale of 2.0 months and explain 8% and 15% of the total variability. These are again identified as barotropic Rossby basin modes.

So, in agreement with the hypothesis stated in the beginning of this section, an internal mode seems to give rise to the simulated low-frequency variability for the coupled wind-driven/DWBC flow, whereas for the

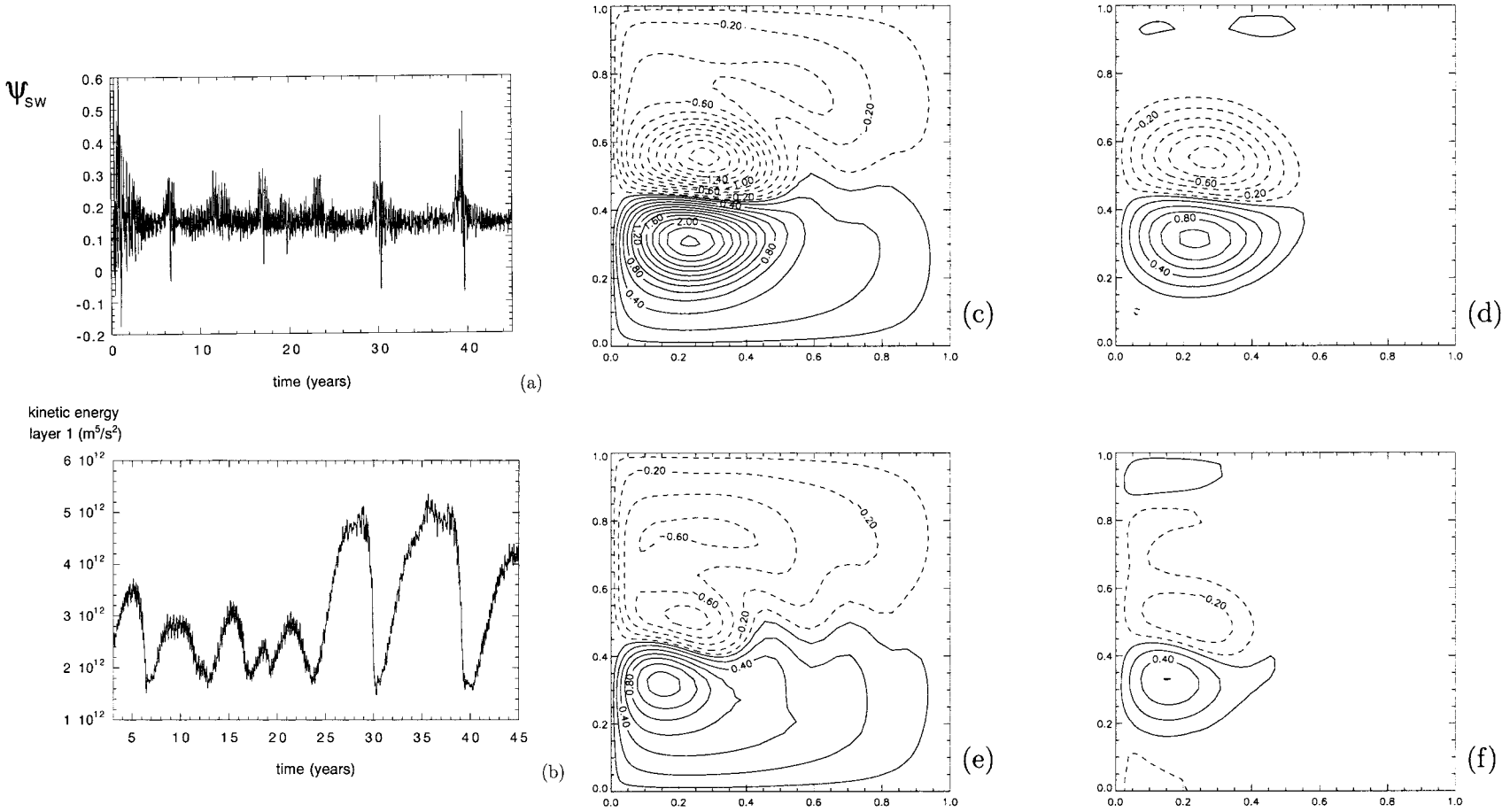

FIG. 10. Time series for (a) ψ_{SW} and (b) the upper-layer kinetic energy, for the purely wind-driven flow ($\Gamma_2^* = 0$) at Re = 130. In (b), only the last 42 years of the total time series (i.e., the part used for the M-SSA analysis) are plotted. [(c)–(f)] Time mean states for the upper and lower layers from the time series in (a), for [(c)–(d)] a high-energy state (average over years 27–29), and [(e)–(f)] a low-energy state (average over years 39–41). Contour interval is 0.2 in plots [(c)–(f)].

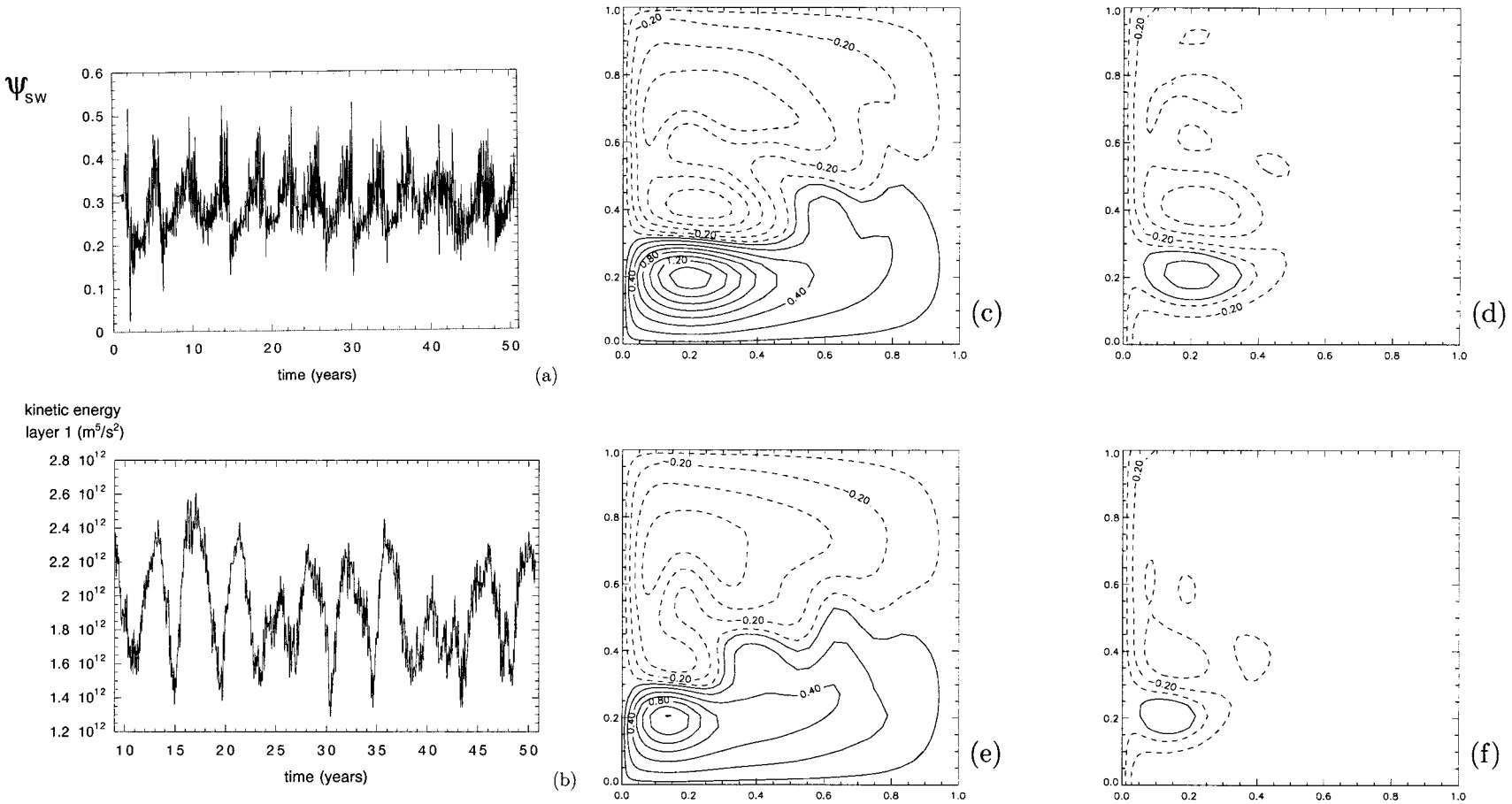

FIG. 11. [(a)–(b)] As in Fig. 10 but for the coupled wind-driven/DWBC flow ($\Gamma_2^* = 7.2$ Sv) at Re = 130. [(c)–(f)] Time mean states for the upper and lower layers from the time series in (a), for [(c)–(d)] a high-energy state (average over years 16–18) and [(e)–(f)] a low-energy state (average over years 38–39). Contour interval is 0.2 in plots [(c)–(f)].

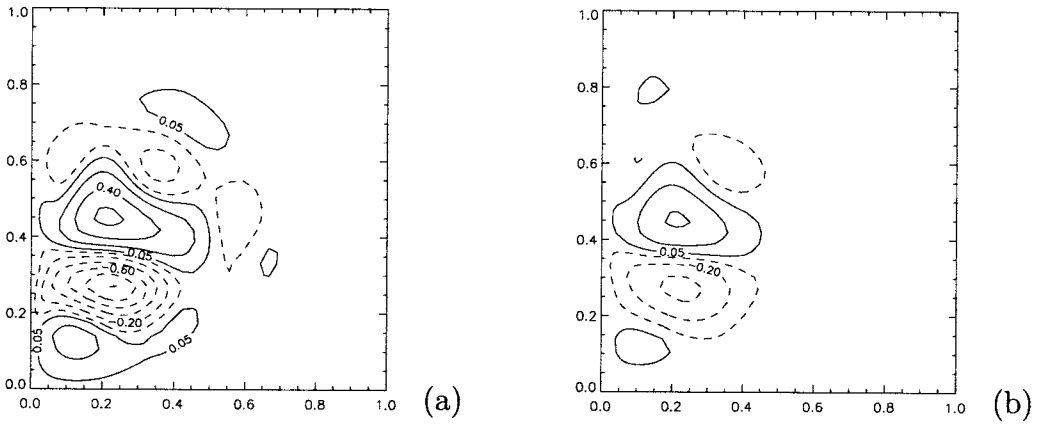

FIG. 12. Snapshot of the spatial pattern of the most dominant statistical mode from the M-SSA analysis of the coupled wind-driven/DWBC flow in Figs. 11a and 11b, in the (a) upper and (b) lower layers. The plots are scaled with the maximum of the field in (a).

purely wind-driven flow the low-frequency variability could not be linked to any known internal mode. More support for this conclusion is obtained by analyzing the spectra of the time series of the upper-layer kinetic energy. For both the coupled wind-driven/DWBC flow and the purely wind-driven flow, this spectrum is shown in Figs. 13a and 13b. On the horizontal axis, the dimensionless frequency f is plotted. The dimensional period p^* (in seconds) associated with a particular frequency f is $p^* = L/(Uf)$. The highest frequency that is resolved if $f = 50$, which corresponds to a period p^* of 2 weeks (two times the sample interval), but only the frequencies $f < 20$ are displayed in this figure ($p^* > 5$ weeks). For $\Gamma_2^* = 7.2$ Sv, a distinct low-frequency peak is found near $f = 0.5$, which corresponds to a period of 4 yr. This is the signature of the dominant mode of variability derived from the M-SSA analysis, which was identified as the mode B_9. Another peak in the spectrum is found near $f = 12$ or $p^* = 2$ months, which is the signal of the barotropic Rossby basin modes. For the purely wind-driven flow, the Rossby basin modes also give a clear signal in the intermonthly frequency band (Fig. 13b). In the low-frequency band, the spectrum has no distinct low-frequency peak. So, the internal mode of variability B_9 appears to dictate the timescale of the low-frequency variability for the coupled wind-driven/DWBC flow, whereas for the purely wind-driven flow there seems to be no preferred low-frequency timescale.

In line with this conclusion, a histogram of the kinetic energy distribution for the coupled wind-driven/DWBC flow does not show a preference for a specific state (Fig. 13c) because during the low-frequency oscillation all values have the same likeliness to occur. On the other hand, for the purely wind-driven flow (Fig. 13d) the distribution shows three distinct peaks, indicative of irregular transitions between the high-, medium-, and low-energy states in Fig. 10b. Unlike for the coupled wind-driven/DWBC flow, for the wind-driven flow the mean value of the kinetic energy is not the one that is visited most often.

The results presented here show that at relatively low friction, in correspondence with McCalpin and Haidvogel (1996), Berloff and McWilliams (1999), and Meacham (2000), low-frequency variability can appear in purely wind-driven flows due to nonlinear interactions of unstable high-frequency modes. At a comparable value of Re, a substantial part of the low-frequency variability in the coupled wind-driven/DWBC flow is caused by an unstable low-frequency mode. We now have an interpretation framework for the results in Spall (1996b) and are in a position to assess the impact of the DWBC on low-frequency variability.

7. Discussion

In this paper, the interactions between the Gulf Stream and a deep western boundary current (DWBC) are studied, focusing on the internal variability of the flow. The main motivation for this study has been to understand results in the paper by Spall (1996b), where decadal variability is found in a numerical model of the Gulf Stream/DWBC system. The reference point chosen is the purely wind-driven flow, and changes in structure of stationary solutions, instabilities, and time-dependent behavior have been monitored using the lateral friction and the strength of the DWBC as control parameters.

For the purely wind-driven flow, the stationary flows are destabilized at large friction through baroclinic instabilities. As a result, intermonthly timescales of variability are introduced. At low friction, nonlinear interactions lead to low-frequency variability through a similar scenario as proposed by Berloff and McWilliams (1999). Transitions between high- and low-energy states are involved in this low-frequency variability, but the M-SSA analysis of the time series indicates that no particular low-frequency oscillatory mode stands out.

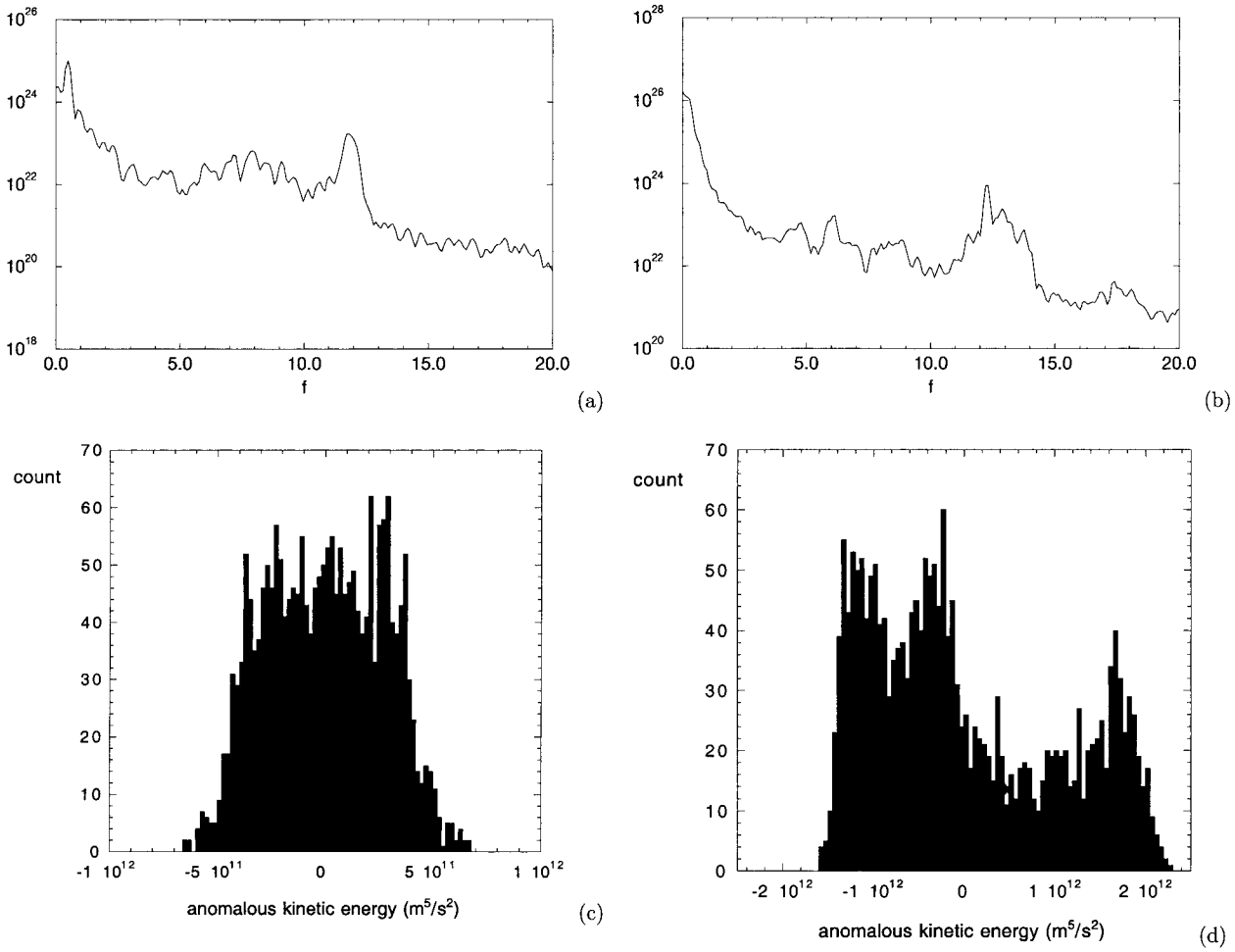

FIG. 13. Spectra of the time series for the upper-layer kinetic energy (a) for the coupled wind-driven/DWBC flow in Fig. 11b and (b) for the purely wind-driven flow in Fig. 10b. On the horizontal axis, the dimensionless frequency f is plotted [the dimensional period $p^* = L/(Uf)$]. The range in f shown here is $f \in [0.0, 20.0]$, corresponding to periods $p^* > 5$ weeks. [(c)–(d)] Histograms of the distribution of the upper-layer kinetic energy with respect to its mean value, (c) for the coupled wind-driven/DWBC flow in Fig. 11b and (d) for the purely wind-driven flow in Fig. 10b. To construct these plots, the range in kinetic energy visited during the 42-yr time series is divided into 100 bins of equal width, and subsequently the number of samples in each bin is counted.

The presence of the DWBC has a significant impact on the characteristics of the wind-driven flow. First, its presence leads to the existence of unique stationary solutions for the coupled Gulf Stream/DWBC flow, whereas multiple stationary solutions were found for the purely wind-driven flow (section 4). Second, its presence strongly favors interannual instabilities (section 5). As was shown by the M-SSA analysis of the time series, the variability at low friction is dominated by one of these instabilities. Through pattern and timescale comparison, it was identified as the internal mode B_9 (section 6).

A comparison of our results with observations of the variability of the Gulf Stream/DWBC system, as described for example by Pickart (1994), does not seem appropriate at this stage. First, we do not expect our idealized model to be capable of capturing the details of the flow. Neglected features like bottom topography and the shape of the coastline will certainly modify the flow, even though they may not be essential to the basic physical mechanisms behind the variability. A second difficulty is that, with respect to the low-frequency variability, the observational records are still simply too short. An interesting issue that can be addressed, however, is whether an internal low-frequency mode like the one discussed in this paper may play a role in the variability of Gulf Stream/DWBC system as modeled by Spall (1996b). In that study, the dominant timescale of variability is 10 yr, considerably longer than the interannual timescale of the low-frequency mode B_9 discussed here. However, the timescale of the mode probably increases with the basin size, which is larger in Spall (1996b) than in this study (3500 km $\times$ 2500 km versus 1000 km $\times$ 1000 km). Tansley and Marshall (2000) also used a quite small basin to study the interactions between the Gulf Stream and the DWBC (2000

km × 1000 km), and mainly found variability on interannual timescales, as in our study.

Next, we can compare the spatial pattern of the mode B_9 at different phases of the oscillation with the extreme phases of the low-frequency oscillation in the 3-layer model described by Spall (1996b). In that model, the Gulf Stream penetrates far into the basin and is flanked by eddy-driven recirculation gyres during the high-energy phase of the oscillation. At intermediate depth, in the second model layer, recirculation gyres exist, which are aligned with the Gulf Stream above. The upper DWBC is entrained into these recirculation gyres. During the opposite phase, when the kinetic energy of the flow is relatively low, the Gulf Stream penetrates less far into the basin. Only part of the upper DWBC is entrained in the (now weaker) recirculation gyres, while part of it is unaffected and continues southward. We can compare these high- and low energy phases with the oscillatory flow that arises by adding the low-frequency mode B_9 (Figs. 7e,f) to the stationary solution for the coupled wind-driven/DWBC flow at high Re (Figs. 8c,d). Adding the low-frequency mode at phase $\hat{t} = 0.0$ (Fig. 7e) weakens the recirculation gyres in the upper layer [the strongest anomalies, near $(x, y) = (0.2, 0.25)$ and (0.2, 0.4), have the opposite sign as the stationary flow]. As a result, the upper-layer jet penetrates less far into the basin. During the opposite phase ($\hat{t} = 0.5$), the sign of the perturbation streamfunction of the mode is reversed, and the recirculation gyres are strengthened. In the lower layer, the perturbation at $\hat{t} = 0.0$ (Fig. 7f) moderates the deflection of the DWBC. The opposite occurs half a period later: the sign of the anomaly reverses, and stronger deflection occurs. So, based on the spatial characteristics, the high- and low-energy phases of the oscillation described by Spall (1996b) resemble the $\hat{t} = 0.5$ and $\hat{t} = 0.0$ phases of the low-frequency internal mode of variability described in this study, respectively. Moreover, the effect of the mode on the separation point of the upper-layer jet is similar. The separation point of the stationary solution is located at $y = 0.28$ (see Fig. 8c). At phase $\hat{t} = 0.5$, the high-energy phase, the upper-layer perturbation streamfunction is positive at that latitude (Fig. 7e) and, hence, the separation point shifts northward during this phase, as in Spall (1996b).

In the transient flows at low friction discussed in section 6, low-frequency variability is found independent of the presence of the DWBC. As was shown in the spectra of the time series, the low-frequency spectral characteristics are quite different in the two situations. In the presence of the DWBC, a single internal mode of variability dominates the low-frequency variability, whereas nonlinear interactions between high-frequency signals are responsible for the low-frequency variability when the DWBC is absent. Since low-frequency variability is found in transient flows under a wide range of parameter settings in different model configurations (McCalpin and Haidvogel 1996; Berloff and McWilliams 1999; Meacham 2000; and this study), all lacking a DWBC, it is in hindsight actually quite surprising that in the study by Spall (1996b) low-frequency variability is absent when the DWBC transport in the second layer is set to zero. It seems unlikely that the presence of the third layer influences the variability characteristics so drastically. Our speculation is that the boundary conditions in the upper layer (i.e., the in- and outflow conditions) affect the stability characteristics of the midlatitude jet. As a consequence, the nonlinear interactions between the baroclinic modes that destabilize this jet may be different for the specific model configuration discussed by Spall (1996b). When these nonlinear interactions of high-frequency modes are relatively weak, it is possible that they do not give rise to low-frequency variability in this particular parameter regime. The low-frequency variability that is found when the upper DWBC is present may be caused by a low-frequency internal mode that is present only for the coupled Gulf Stream/DWBC flow, in a similar way as discussed in this paper.

To be able to compare the results discussed here with those presented in Dijkstra and Katsman (1997), the same set of parameter values was used in both studies. However, the chosen depth of the second layer is relatively shallow, which results in quite vigorous interaction between the wind-driven gyres and the DWBC. Therefore, the sensitivity of the results to the depth of the second layer was investigated shortly, in particular with regard to the stability of the low-frequency internal mode B_9. This mode was traced at low friction (Re = 125) while increasing D_2 from its standard value of 1400 m. Two cases were considered. First, we kept the DWBC transport Γ_2^* fixed at 7.2 Sv, by simultaneously decreasing V_{in} while increasing D_2. This appeared to have little impact on the stability of the mode B_9, as its growth rate remained close to criticality. Its timescale varied between 4 and 5 yr, depending on the exact value of D_2. Second, D_2 was increased while keeping V_{in} constant. As a consequence, Γ_2^* increased with D_2. This was found to destabilize B_9 considerably, whereas its period still remained approximately 5 yr. So, we are confident that the existence of this unstable low-frequency internal mode is robust for larger depths of the second layer.

Acknowledgments. The authors would like to thank Maurice Schmeits (IMAU) for performing the M-SSA analysis of the transient flows. This research was supported by the Netherlands Organization for Scientific Research (NWO) through project 620-61-353 of the program Niet-Lineaire Systemen (Non-Linear Systems). All computations were performed on the CRAY C98 at the Academic Computer Centre (SARA), Amsterdam, The Netherlands, within the project SC498. Use of these computing facilities was sponsored by the National Computing Facilities Foundation (NCF) with financial

support from the Netherlands Organization of Scientific Research (NWO).

REFERENCES

Berloff, P. S., and S. P. Meacham, 1998: On the stability of the wind-driven circulation. *J. Mar. Res.*, **56,** 937–993.

——, and J. C. McWilliams, 1999: Large-scale, low-frequency variability in wind-driven ocean gyres. *J. Phys. Oceanogr.*, **29,** 1925–1949.

Bower, A. S., and H. D. Hunt, 2000a: Lagrangian observations of the deep western boundary current in the North Atlantic Ocean. Part I: Large-scale pathways and spreading rates. *J. Phys. Oceanogr.*, **30,** 764–783.

——, and ——, 2000b: Lagrangian observations of the deep western boundary current in the North Atlantic Ocean. Part II: The Gulf Stream–deep western boundary current crossover. *J. Phys. Oceanogr.*, **30,** 784–804.

Dijkstra, H. A., and C. A. Katsman, 1997: Temporal variability of the wind-driven quasi-geostrophic double gyre ocean circulation: Basic bifurcation diagrams. *Geophys. Astrophys. Fluid Dyn.*, **85,** 195–232.

——, and M. J. Molemaker, 1999: Imperfections of the North-Atlantic wind-driven ocean circulation: Continental geometry and wind-stress. *J. Mar. Res.*, **57,** 1–28.

——, ——, A. van der Ploeg, and E. F. F. Botta, 1995: An efficient code to compute nonparallel flows and their linear stability. *Comput. Fluids*, **24,** 415–434.

——, M. J. Schmeits, and C. A. Katsman, 1999: Variability of the North Atlantic wind-driven ocean circulation. *Surv. Geophys.*, **20,** 463–503.

Hogg, N. G., 1983: A note on the deep circulation of the western North Atlantic: Its nature and its causes. *Deep-Sea Res.*, **30,** 945–961.

Jiang, S., F. F. Jin, and M. Ghil, 1995: Multiple equilibria and aperiodic solutions in a wind-driven double-gyre, shallow-water model. *J. Phys. Oceanogr.*, **25,** 764–786.

Katsman, C. A., H. A. Dijkstra, and S. S. Drijfhout, 1998: The rectification of wind-driven flow due to its instabilities. *J. Mar. Res.*, **56,** 559–587.

McCalpin, J. D., and D. B. Haidvogel, 1996: Phenomenology of the low-frequency variability in a reduced-gravity, quasigeostrophic double-gyre model. *J. Phys. Oceanogr.*, **26,** 739–752.

Meacham, S. P., 2000: Low-frequency variability in the wind-driven circulation. *J. Phys. Oceanogr.*, **30,** 269–293.

Nayfeh, A. H., and B. Balachandran, 1995: *Applied Nonlinear Dynamics.* John Wiley and Sons, 685 pp.

Pedlosky, J., 1987: *Geophysical Fluid Dynamics*. 2d ed. Springer-Verlag, 710 pp.

——, 1996: *Ocean Circulation Theory*. Springer Verlag, 453 pp.

Pickart, R. S., 1994: Interaction of the Gulf Stream and Deep Western Boundary Current where they cross. *J. Geophys. Res.*, **99**(C12), 25 155–25 164.

——, and W. M. Smethie Jr., 1993: How does the deep western boundary current cross the Gulf Stream? *J. Phys. Oceanogr.*, **23,** 2602–2616.

——, and ——, 1998: Temporal evolution of the Deep Western Boundary Current where it enters the sub-tropical domain. *Deep-Sea Res. I,* **45,** 1053–1083.

Plaut, G., and R. Vautard, 1994: Spells of low-frequency oscillations and weather regimes in the Northern Hemisphere. *J. Atmos. Sci.*, **51,** 210–236.

Qiu, B., 2000: Interannual variability of the Kuroshio Extension system and its impact on the wintertime SST field. *J. Phys. Oceanogr.*, **30,** 1486–1502.

Richardson, P. L., 1977: On the crossover between the Gulf Stream and the western boundary undercurrent. *Deep-Sea Res.*, **24,** 139–159.

Schmeits, M. J., and H. A. Dijkstra, 2000: Physics of the 9-month variability in the Gulf Stream region: Combining data and dynamical systems analyses. *J. Phys. Oceanogr.*, **30,** 1967–1987.

Spall, M. A., 1996a: Dynamics of the Gulf Stream/deep western boundary current crossover. Part I: Entrainment and recirculation. *J. Phys. Oceanogr.*, **26,** 2152–2168.

——, 1996b: Dynamics of the Gulf Stream/deep western boundary current crossover. Part II: Low-frequency internal oscillations. *J. Phys. Oceanogr.*, **26,** 2169–2182.

Speich, S., H. A. Dijkstra, and M. Ghil, 1995: Successive bifurcations of a shallow water model, applied to the wind-driven circulation. *Nonlinear Proc. Geophys.*, **2,** 241–268.

Tansley, C. E., and D. P. Marshall, 2000: On the influence of bottom topography and the Deep Western Boundary Current on Gulf Stream separation. *J. Mar. Res.*, **58,** 297–325.

Thompson, J. D., and W. J. Schmitz Jr., 1989: A limited-area model of the Gulf Stream: Design, initial experiments and model–data comparison. *J. Phys. Oceanogr.*, **19,** 791–814.